we adopted in this study.

5. J. M. Lees, *Geophys. Res. Lett.* **17**, 1433 (1990); J. M. Lees and C. E. Nicholson, *Geology* **21**, 387 (1993); W. Foxall, A. Michelini, T. V. McEvilly, *J. Geophys. Res.* **98**, 17691 (1993); D. Zhao and H. Kanamori, *Geophys. Res. Lett.* **20**, 1083 (1993); *ibid* **22**, 763 (1995).

6. D. Eberhart-Phillips and A. J. Michael, *J. Geophys. Res.* **98**, 15737 (1993); P. A. Johnson and T. V. McEvilly, *ibid.* **100**, 12937 (1995); G. S. Fuis *et al.*, *Eos* **77**, 173 (1996).

7. H. K. Gupta, S. V. S. Sarma, T. Harinarayana, G. Virupakshi, *Geophys. Res. Lett.* **23**, 1569 (1996). Seismologic and magnetotelluric studies revealed a low-velocity, high conductive anomaly near the hypocenter of the 1993 Latur earthquake in India. The anomaly was interpreted as a fluid-filled, fractured rock matrix that may have contributed to the nucleation of the Latur earthquake.

8. D. Zhao, A. Hasegawa, S. Horiuchi, *J. Geophys. Res.* **97**, 19909 (1992). We set up a 3D grid in the study area with a grid spacing of 4 to 5 km in the horizontal direction and 2 to 4 km in depth. Hypocenter locations and velocities at the grid nodes are taken as unknown parameters. The velocity at any point in the model is calculated by linearly interpolating the velocities at the eight grid nodes surrounding that point. An efficient 3D ray tracing technique is used to compute travel times and ray paths. We used a conjugate gradients algorithm to invert the large and sparse system of observation equations that relate the observed arrival-time data to the unknown parameters. P- and S-wave velocity structure and hypocenter parameters are simultaneously determined in an iterative inversion process. Then we use the relation $(V_p/V_s)^2 = 2(1 - \sigma)/(1 - 2\sigma)$, to determine σ distribution. The tomographic inversion was conducted for the area shown in Fig. 1. Only the ray paths within that area were used in the inversion. We did not use station corrections in our parameterization; any local anomalies close to stations can be resolved as velocity anomalies at the grid nodes of the top grid mesh layer at a depth of 0 km. Elevations of stations are included in the 3D ray tracing. The initial one-dimensional velocity model consists of four layers that are separated by the Conrad and Moho discontinuities and a velocity boundary at a depth of 3 km. In the four layers, V_p is 4.8, 6.0, 6.7, and 7.8 km/s. V_p/V_s ratio is 1.73. The Conrad discontinuity is at a depth of 15 to 17 km, and the Moho is at a depth of 34 to 35 km in the Kobe area (D. Zhao, S. Horiuchi, A. Hasegawa, *Tectonophysics* **212**, 289 (1992)). We have taken into account the Conrad and Moho depth changes in the tomographic inversions and found that the velocity changes due to the Conrad and Moho depth variations are less than 0.5% in the tomographic images (Figs. 2 through 4).

9. D. Zhao, H. Kanamori, D. Wiens, H. Negishi, *Eos (fall suppl.)* **76**, 378 (1995).

10. Fault zones are typically less than 1 km wide and composed of highly fractured material, fault gouge, and fluids; see C. H. Scholz, *Geology* **15**, 493 (1987); S. Cox and C. H. Scholz, *J. Struct. Geol.* **10**, 413 (1988); and C. B. Forster and J. P. Evans, *Geophys. Res. Lett.* **18**, 979 (1991). Since the spacing of grid nodes used in our tomographic inversion is 4 to 5 km, the Kobe earthquake fault zone was imaged as a low-velocity zone not narrower than 4 km.

11. N. Hirata *et al.*, *Proc. 1996 Japan Earth Planet. Sci. Meet.*, 38 (1996); N. Tsumura *et al.*, *ibid.*, p. 39.

12. R. J. O'Connell and B. Budiansky, *J. Geophys. Res.* **79**, 5412 (1974); M. N. Toksoz, C. H. Cheng, A. Timur, *Geophysics* **41**, 621 (1976); D. Moos and M. D. Zoback, *J. Geophys. Res.* **88**, 2345 (1983).

13. To make a checkerboard, we assigned positive and negative velocity anomalies to the 3D grid nodes. Synthetic data are calculated for the checkerboard model. Then we added random errors of 0.05 to 0.15 s to the synthetic data and inverted them with the same algorithm as we did for the observed data. The inverted image of the checkerboard suggests where the resolution is good and where it is poor.

14. Y. Mamada *et al.*, *Progr. Abstr. Fall Meet. Seismol. Soc. Japan*, P37 (1995).

15. E. Fukuyama, *ibid.*, p. A87; K. Tadokoro, Y. Umeda, M. Ando, *Proc. 1996 Japan Earth Planet. Sci. Meet.*, 44

(1996). The direction of the fastest S waves is generally oriented east-west in the Nojima fault zone. The time difference between the two splitting S waves is generally 0.1 s and does not exceed 0.15 s. This means that the effect of S-wave splitting on the accuracy of S-wave arrival-time data is not larger than 0.15 s.

16. K. Ito, Y. Umeda, S. Ohmi, A. Ohigashi, K. Matsumura, *Progr. Abstr. Fall Meet. Seismol. Soc. Japan*, A79 (1995).

17. Y. Umeda, T. Yamashita, K. Ito, H. Horikawa, *ibid.*, p. A78.

18. H. Katao, N. Maeda, Y. Hiramatsu, Y. Iio, S. Nakao, *ibid.*, p. A74.

19. K. Obara *et al.*, *Proc. 1996 Japan Earth Planet. Sci. Meet.*, 46 (1996); S. Matsumoto *et al.*, *ibid.*, p. 46.

20. S. N. Chatterjee, A. M. Pitt, H. M. Iyer, *J. Volcanol. Geotherm. Res.* **26**, 213 (1985); M. C. Walck, *J. Geophys. Res.* **93**, 2047 (1988); A. Hasegawa and D. Zhao, in *Magmatic Systems*, M. P. Ryan, Ed. (Academic Press, San Diego, 1994), pp. 179–195.

21. I. Yokoyama, S. Aramaki, K. Nakamura, *Volcanoes* (Iwanami Press, Tokyo, 1987).

22. Y. Okubo, H. Tsu, K. Ogawa, *Tectonophysics* **159**, 279 (1989).

23. R. Kerrich, T. E. La Tour, L. Willmore, *J. Geophys. Res.* **89**, 4331 (1984). Fluids may exist in the middle to lower crust in fault zone environments.

24. K. Hirahara, *Tectonophysics* **79**, 1 (1981); D. Zhao, A. Hasegawa, H. Kanamori, *J. Geophys. Res.* **99**, 22313 (1994).

25. R. H. Sibson, in *Earthquake Prediction: An International Review, Maurice Ewing Ser.*, vol. 4, D. W. Simpson, P. G. Richards, Eds. (American Geophysical Union, Washington, DC, 1981), pp. 593–603; R. H. Sibson, *Tectonophysics* **211**, 283 (1992); S. Hickman, R. H. Sibson, R. Bruhn, *J. Geophys. Res.* **100**, 12831 (1995).

26. We are grateful to the members of the Urgent Observation Group for the 1995 Hyogo-Ken Nanbu Earthquake, who operated the portable stations and picked the P- and S-wave arrival times, and to the staff members of the seismic networks of Kyoto University, Nagoya University, Kochi University, Kyushu University, and the University of Tokyo for providing the data recorded by their permanent networks that were used in this study. J. Vidale and an anonymous referee provided thoughtful reviews, which improved the manuscript. This work was partially supported by a grant from the National Science Foundation (EAR-9526810) to D. Zhao. This paper is Contribution 5785, Division of Geological and Planetary Sciences, California Institute of Technology.

4 September 1996; accepted 19 November 1996

Paleontology and Chronology of Two Evolutionary Transitions by Hybridization in the Bahamian Land Snail *Cerion*

Glenn A. Goodfriend and Stephen Jay Gould

The late Quaternary fossil record of the Bahamian land snail *Cerion* on Great Inagua documents two transitions apparently resulting from hybridization. In the first, a localized modern population represents the hybrid descendants of a 13,000-year-old fossil form from the same area, introgressed with the modern form now characteristic of the adjacent regions. In the second case, a chronocline spanning 15,000 to 20,000 years and expressing the transition of an extinct fossil form to the modern form found on the south coast was documented by morphometry of fossils dated by amino acid racemization and radiocarbon. Hybrid intermediates persisted for many thousands of years.

Most evolutionary transitions between species are trapped in a no man's land of invisibility. Such events generally require too much time for direct observation but occupy too short an interval for preservation in the fossil record. However, favorable circumstances can provide visibility in fortunate instances. We report two cases of radiometrically dated evolution during the past 20,000 years in the land snail *Cerion*, an exceptionally labile genus that produced several stable and novel populations by the rapid mechanism of hybridization (*1*).

Our perspective on the evolution of hybrid zones has generally been based on either (i) very short periods of human observation, typically related to species introductions or habitat disturbance by humans (*2*) or (ii) scenarios inferred from knowledge of climatic

changes and their probable role in bringing different populations into contact [for example, probable postglacial origins of hybrid zones in fire-bellied toads (*3*) or grasshoppers (*4*)]. In the present study, by contrast, we provide direct fossil evidence for the history of older and more persistent hybrid zones.

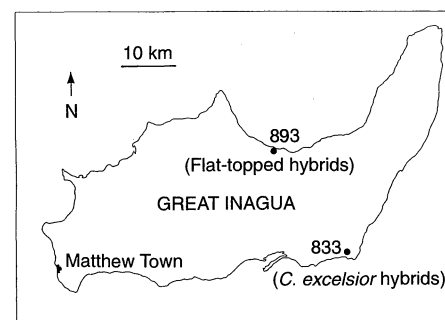Great Inagua (Fig. 1), the largest island of the southeastern Bahamas, is now inhab-

G. A. Goodfriend, Geophysical Laboratory, Carnegie Institution of Washington, 5251 Broad Branch Road, NW, Washington, DC 20015, USA.
S. J. Gould, Museum of Comparative Zoology, Harvard University, Cambridge, MA 02138, USA.

Fig. 1. Map of Great Inagua, showing location of sampling sites.

Fig. 2. Photograph of modern and fossil *Cerion* from the north coast of Inagua. The left two are modern *C. columna* (locality 853); the middle two are modern flat-topped forms of intermediary morphology [locality 892 (5)]; and the right two are fossil flat-topped forms (locality 893). Scale bar is 1 cm.

ited by three species of *Cerion* (5): (i) the smooth, white, and triangular *C. columna* of the northern coastline, (ii) the ribby, brown-mottled, and red-topped *C. rubicundum* of the southern coast and island interior, and (iii) the ubiquitous dwarf *C. rehderi*, living sympatrically with both of the other species. Pleistocene and Holocene deposits of Great Inagua yield at least two other species: the large, smooth, tall, and parallel-sided *C. excelsior* (the largest of all *Cerion* species), extensively distributed over southern Inagua, and a large, flat-topped form, probably an immigrant from the nearby eastern Cuban *C. dimidiatum* complex, known on Inagua only from late Pleistocene rocks in one locality on the northern shore (5) (Fig. 1). Both of these fossil species show direct temporal evidence of hybridization with the living *Cerion* species now resident in their former areas of habitation.

Case one: The flat-topped "area effect" in modern *C. columna.* Although somewhat variable in size, thickness, and ribbing, *C. columna* (Fig. 2) shows no departure throughout its geographic range from the definitive form of a high and narrow apex and generally triangular cross section. However, in one restricted region of the north coast, extending for 3 to 5 km of the total 80-km coastal range of *C. columna,* shells possess a strongly flattened apex otherwise unknown in the species. To both the east and west, shells undergo a rapid

transition to ordinary forms. This flat-topped "area effect" (6) occurs in the same region that has yielded the even flatter topped fossils of the *C. dimidiatum* complex. The modern flat-topped *C. columna* from the area effect are smoothly intermediate between the fossil *C. dimidiatum* and ordinary high-spired populations of *C. columna,* both in general form (Fig. 2) and in distinctive patterns of covariation, as revealed by multivariate analysis of the shells. In addition, three alleles otherwise unknown in *C. columna* have been found at low frequency in the flat-topped area effect population. For these reasons of geography, morphometrics, and genetics, we infer that the area effect population owes its uniquely flat-topped form to retained influence by introgression from the *C. dimidiatum* propagule, now extinct; the area effect represents a hybrid population (5). The fossil propagule has been radiocarbon dated to 13,070 years before present (Table 1). Persistence of hybrid effects over several generations for small propagules swamped by native forms has been demonstrated in *Cerion* before (1), but only for experiments done in this century. These fossils show that the morphometric effects of hybridity from a parental source can persist for many thousands of years after the extinction of a source population.

Case two: The gradual loss of *C. excelsior* influence over 20,000 years in a southern Inaguan population of *C. rubicundum.* Where-

as our first case rests on firm inference but not on direct documentation of the morphological transition, our second case provides fossil evidence of such a transition. The fossil species *C. excelsior,* the distinctive and strikingly large, parallel-sided species of adjacent islands in the southern Bahamas (Inagua, Mayaguana, and East Plana Cay) (7), occurs both in Holocene sediments and in a broad expanse of long-dead shells on sandy silt flats behind the beaches of southern Inagua. In one location (Fig. 1), now inhabited by abundant *C. rubicundum,* thousands of highly variable shells (both in form and preservation) lie exposed on such an extensive flat. These shells span a full range of form, from pure *C. excelsior,* through intermediates of all degrees, to shells indistinguishable from living *C. rubicundum.* Moreover, on visual inspection, the pure *C. excelsior* shells appear most weathered and eroded and generally have heavy secondary carbonate encrustations, whereas pure *C. rubicundum* shells look fresh and unaltered; shells of intermediate forms seem to be weathered to an intermediate degree.

These impressions suggest that the *C. excelsior* population may have initially hybridized with invading *C. rubicundum* (a species unknown in the fossil record of Inagua despite its remarkable current spread and abundance). Eventually all morphological influence from the now extinct *C. excelsior* was lost, as *C. rubicundum* colonized southern Inagua so successfully and extensively. We cannot confirm this conjecture without independent evidence of age, for all specimens lie exposed and in no stratigraphic order. We therefore assessed the smooth morphocline from *C. excelsior* to *C. rubicundum* by multivariate biometry (7) and then established the chronocline by radiometric and amino acid dating methods.

For dating, we selected 19 fossil shells spanning a full range of morphology from the complete sample of 70 specimens (60 fossil and 10 modern) used for the morphometric study. The chronology of the *Cerion* shell samples was determined by a combination of

Table 1. Radiocarbon ages of fossil *Cerion* samples from sites SJG833 and SJG893 on Inagua. Analysis by accelerator mass spectrometry. The ^{14}C ages [in years before present (B.P.)] were adjusted for isotopic fractionation according to equation 8 in (15). These ages were corrected for an age anomaly estimated at 1020 ± 430 years (from Table 2). The calibrated ages are calendric ages determined with CALIB 3.0 (12).

Sample	Site	^{14}C age (years B.P.)	Corrected ^{14}C age (years B.P.)	Calibrated age (cal years B.P.)
CAMS-14234	SJG833	3,930 (±60)	2,910 (±430)	3,040 (±520)
CAMS-14236	SJG833	5,490 (±60)	4,470 (±430)	5,000 (±520)
CAMS-14235	SJG833	14,890 (±70)	13,870 (±440)	16,640 (±560)
AA-7658	SJG893	12,180 (±115)	11,160 (±445)	13,070 (±570)

Table 2. Radiocarbon analyses of prebomb Bahamian *Cerion* from the U.S. National Museum of Natural History collection, collected live in 1930 (year uncertain for the Inagua sample). The ^{14}C was corrected for isotopic fractionation according to equation 8 in (15). The anomaly was calculated relative to a value of 150 years B.P., the radiocarbon age of atmospheric carbon in 1930 (16). Conventional analysis by ethane gas proportional counting was performed at the Weizmann Institute of Science radiocarbon laboratory.

Locality	^{14}C age (years B.P.)	Anomaly (years)
Inagua	1770 (±45)	1520
North side, Margach Cay	890 (±55)	740
West shore, Anguilla Cay	960 (±45)	810

radiocarbon and amino acid racemization (D-alloisoleucine/L-isoleucine, or A/I) analyses (8). We used racemization analysis to obtain a relative chronology of the individual shells because A/I values increase with age. This relative chronology could then be tied to an absolute chronology through radiocarbon dating of three individuals selected to span the full range of morphology and preservation: a pure *C. excelsior*, an intermediate, and the fossil shell closest to modern *C. rubicundum* (Table 1). This approach has been used to resolve the chronology of shells from mixed-age deposits in a variety of contexts (9).

The radiocarbon ages of land snail shells in limestone areas are anomalously old as a result of the ingestion of ancient carbonate (deficient in ^{14}C) by the snails and its subsequent incorporation into the shell during growth (10). To evaluate the extent of this radiocarbon age anomaly in *Cerion* shells, we carried out radiocarbon analyses on several sets of shells collected alive before thermonuclear bomb tests in the 1950s altered atmospheric ^{14}C levels (11). Results (Table 2) indicate a mean age anomaly of 1020 years, with a standard deviation of 430 years. Consequently, we subtracted this mean value from measured ^{14}C ages of fossil samples and then summed the variance with the reported analytical variance of the ^{14}C age to obtain the overall uncertainty of the ^{14}C age. We then converted these corrected radiocarbon ages to calendric ages (12).

We performed a factor analysis on the 70 fossil and modern shells, using 18 variables of our standard protocol (13) to express the major features, allometries, and covariances in the growth of *Cerion* (protoconch dimensions, whorl numbers and sizes, apertural size and orientation, and adult shell size and shape; we omitted measures of ribbing, which could not be reliably determined on many of the eroded

fossils). Three varimax axes of a Q-mode analysis on variables equally weighted by a percent-range transformation encompassed 94.6% of the information.

The first axis expressed the common growth allometry of all *Cerion* (as shown by factor scores for the 18 variables) and made no temporal distinction among shells (as indicated by a lack of correlation between factor loadings for specimens and the measured A/I ratios). This first axis expresses the negative interaction of measures for whorl numbers and standardized whorl sizes—a constraint that we have called the "jigsaw covariance" (14) to express the geometric necessity that shells can reach a common adult size with either fewer large whorls or more smaller whorls—thus producing the negative interaction of whorl sizes and numbers. Because all *Cerion* grow under this constraint, the two end member species of this analysis are not distinguished on this axis.

The second axis (36.5%) expresses all of the essential measured differences between *C. excelsior* and *C. rubicundum*. Six variables score above 0.2 on this axis. These, and only these, mark the basic conchological differences between the two species. Shells of *C. excelsior* are larger by addition of more whorls, which (under *Cerion*'s standard allometry) add height with little augmentation of width (shell height scores 0.548 on the second axis, and width only 0.279). As the second major distinction (Fig. 3), the aperture of *C. excelsior* is more strongly inclined and tilted away from the axis of coiling, whereas the aperture of *C. rubicundum* grows in greater continuity with preceding whorls (three measures of apertural shape and orientation score from 0.320 to 0.410 on the second axis). Finally, the greater twist of *C. excelsior*'s aperture necessarily produces a larger umbilicus (umbilical width

scores 0.306). By contrast, the nine measures of protoconch and whorl sizes do not distinguish the two species and therefore score near zero on the second axis (range of −0.092 to +0.122 with a mean of +0.020).

As expected, pure *C. excelsior* specimens load with the highest values on axis 2, and modern *C. rubicundum* shells load with the lowest values. The intermediate fossils load with values between those of these end-members (Fig. 3). When plotted in relation to a relative time axis, as represented by A/I values, a clear temporal trend in morphology emerges. Simple linear regression of the factor axis 2 loading against A/I values for all specimens (fossil and modern) confirms this trend (two-tailed test for slope = 0: t = 7.9, $P < 0.0001$); fossils alone also yield a highly significant trend (t = 6.1, $P < 0.0001$). The R^2 values (0.69 and 0.68, respectively) indicate that about two-thirds of the axis 2 variation in the samples can be ascribed to temporal change.

The two highest loadings (pure *C. excelsior* by appearance) are the oldest shells by A/I values; the seven lowest loadings are for modern shells. We conclude that the intermediate loadings of all fossils with intermediate ages record the hybridization of *C. rubicundum* immigrants with an original *C. excelsior* stock and the gradual waning of *C. excelsior* influence as this fossil species died out and *C. rubicundum* spread over Inagua to its current abundance. We do not have enough data to discern the fine-scale pattern of intermediacy, in particular, whether the waning of *C. excelsior* influence occurred continually or in plateaus. Because one of the older intermediate specimens is 16,600 years old and the youngest is 3000 years old, we conclude that the morphometric effects of hybridity endured for at least 13,000 years, thus providing a striking example for substantial persistence, with long-extended intermediacy, of an evolutionary phenomenon often viewed as far more evanescent. Hybrid zones may, of course, endure this long and far longer as dynamic entities between two persisting end members, but the extinction of an end member must sever one end of the balance and should spell rapid elimination of hybrids unless the mixed population evolves selected developmental and genetic uniquenesses of its own, thus permitting the production of stable novelty by hybridization.

In favorable circumstances such as these, the fossil record can supply direct evidence for evolutionary change at the generational scales of microevolutionary processes, rather than the conventional paleontological scale of general trends over millions of years. The usual broad brush represents a fascinating scale in its own macroevolutionary right, but it cannot resolve the blips and fillips that
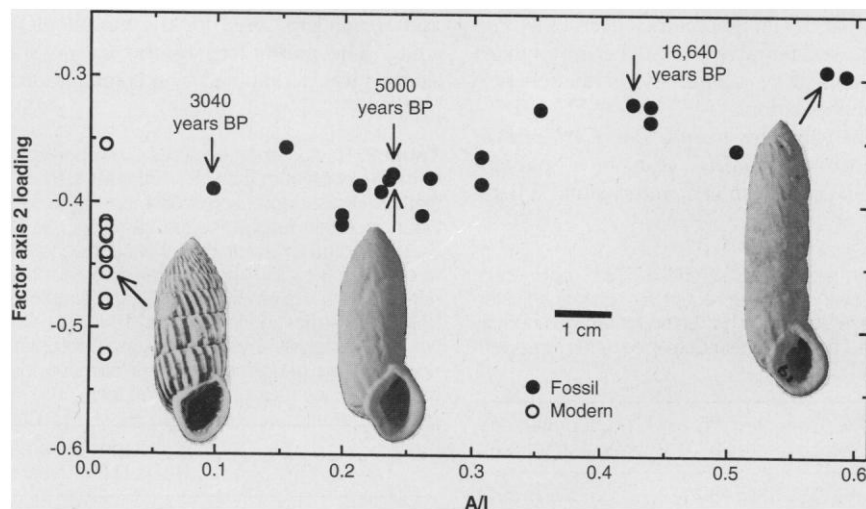

Fig. 3. Shell morphology of fossil and modern *Cerion* shells from site SJG833 (as expressed by loadings on factor axis 2) in relation to age (as indicated by A/I values). Radiocarbon ages (from Table 2) for three of the shells are indicated. Scale refers to shell photographs.

mark the richness of life's history and constitute the only scale of evolution directly observable in our own historic time. The *Cerion* fossil record thus supplies an empirical bridge between these two crucial scales of evolution.

REFERENCES AND NOTES

1. D. S. Woodruff and S. J. Gould, *Evolution* **41**, 1022 (1987); P. Bartsch, *Carnegie Inst. Washington Yearbk.* **20**, 198 (1922); *ibid.* **30**, 373 (1931).
2. N. H. Barton and G. M. Hewitt, *Annu. Rev. Ecol. Syst.* **16**, 113 (1985).
3. J. M. Szymura, in *Hybrid Zones and the Evolutionary Process*, R. G. Harrison, Ed. (Oxford Univ. Press, New York, 1993), pp. 261–289.
4. G. M. Hewitt, *ibid.*, pp. 140–164.
5. S. J. Gould and D. S. Woodruff, *Biol. J. Linn. Soc.* **40**, 67 (1990).
6. "Area effects," as originally defined by A. J. Cain and J. D. Currey [*Philos. Trans. R. Soc. London* **246**, 1 (1963)], occur in geographic regions housing distinctive local populations of a species (in an area larger than that of a panmictic population) where sharp borders separate the population from other distinctive populations of the species but where no evident feature of climate, habitat, or ecology correlates with the sharp change in phenotype. This phenomenon is common in land snails and has generated a large literature, reviewed in (5).
7. S. J. Gould, *Paleobiology* **10**, 172 (1984).
8. After cleaning and hydrolysis (in 6 N HCl at 100°C for 20 hours), samples were desalted with HF and analyzed by high-pressure liquid chromatography, with the use of postcolumn *o*-phthaldialdehyde derivatization [P. E. Hare, P. A. St. John, M. H. Engel, in *Chemistry and Biochemistry of the Amino Acids*, G. C. Barrett, Ed. (Chapman & Hall, London, 1985), p. 415]. Peak area ratios were calibrated against a standard A/I mixture. Errors averaged ±4% of the A/I value.
9. G. A. Goodfriend, *Radiocarbon* **31**, 1041 (1989); _____ and R. M. Mitterer, *Geol. Soc. Am. Bull.* **105**, 18 (1993); G. A. Goodfriend, R. A. D. Cameron, L. M. Cook, *J. Biogeogr.* **21**, 309 (1994); G. A. Goodfriend and D. J. Stanley, *Mar. Geol.* **129**, 271 (1996).
10. G. A. Goodfriend and J. J. Stipp, *Geology* **11**, 575 (1983).
11. A. A. Burchuladze *et al.*, *Radiocarbon* **31**, 771 (1989).
12. M. Stuiver and P. J. Reimer, *ibid.* **35**, 215 (1993).
13. S. J. Gould and D. S. Woodruff, *Bull. Am. Mus. Nat. Hist.* **182**, 389 (1986).
14. S. J. Gould, *Evolution* **43**, 516 (1989).
15. G. A. Goodfriend, *Radiocarbon* **29**, 159 (1987).
16. M. Stuiver and G. W. Pearson, *ibid.* **28**, 805 (1986).
17. Laboratory facilities were provided by P. E. Hare, and conventional radiocarbon dates, by I. Carmi. We thank B. Robinson for making measurements and performing biometrical analyses. R. Herschler of the U.S. National Museum of Natural History provided prebomb *Cerion* for radiocarbon analysis. We thank D. S. Woodruff for his role in the fieldwork.

Nanocapillarity and Chemistry in Carbon Nanotubes

D. Ugarte,* A. Châtelain, W. A. de Heer

Open carbon nanotubes were filled with molten silver nitrate by capillary forces. Only those tubes with inner diameters of 4 nanometers or more were filled, suggesting a capillarity size dependence as a result of the lowering of the nanotube-salt interface energy with increasing curvature of the nanotube walls. Nanotube cavities should also be less chemically reactive than graphite and may serve as nanosize test tubes. This property has been illustrated by monitoring the decomposition of silver nitrate within nanotubes in situ in an electron microscope, which produced chains of silver nanobeads separated by high-pressure gas pockets.

The nanoscale cavities of fullerenes (1) and nanotubes (2) may be used for generating encapsulated compounds or elongated nanostructures. Early attempts to fill fullerene-related materials were based on the electric arc method, in which graphite electrodes were impregnated with the filling material (3–5). These experiments led to the discovery of a variety of filled graphitic structures (6–8); however, the abundances of filled structures were very low and their production was difficult to control. Alternatively, nanotube production and filling procedures can be separated by using efficient nanotube production methods (9) and by utilizing capillary forces (10–13) for filling them. Dujardin *et al.* (11) have shown that elements and compounds that wet graphite (that is, with surface tensions of ≤190 mN/m) are potential candidates for nanotube-filling materials. More recently, a simple wet chemical method was developed for the opening and filling of nanotubes, which facilitates the inclusion of a wide variety of materials (14). The tubes are treated with diluted nitric acid in which a metal salt is dissolved; once a tube has been opened, the liquid enters the nanotube, and the formation of enclosed metal oxide particles can be induced by a subsequent calcinating step. A drawback of this method is that initially the nanotube is filled mostly with the solvent.

To resolve this and other problems, we have developed a four-step procedure involving: (i) synthesis of the tubes, (ii) opening, (iii) high-temperature annealing, and (iv) capillary filling with a molten pure metal salt such as $AgNO_3$ (15). It was verified that in the case of $AgNO_3$, the molten salt entered the tubes. In some cases, the tubes were filled along their entire length (16). Metallization of the encapsulated salt was induced by the electron beam in an electron microscope, which was used to monitor the chemical reactions inside the tube. The results presented here illustrate several processes occurring in the nanotube cavities, namely: (i) the filling process (capillarity and wetting), (ii) the metallization (decomposition of silver nitrate and silver bead formation), and (iii) chemical reactions between evolved gases and the nanotube interior.

The filling efficiency (~2 to 3%) is much lower than the efficiency to open tube tips by oxidation (~60%), resulting in only a small fraction of the opened tubes being filled. The inner diameter distribution of the nanotubes peaks at ~2 nm (Fig. 1A), but the filled tube cavities are usually those with a large inner diameter (≥4 nm), and filling of small diameter tubes (1 to 2 nm) was not observed (Fig. 1B). The low percentage of filled nanotubes thus simply reflects the low abundance of large inner diameter tubes, the majority of which were filled. Similar filling diameters were also observed by others using various

D. Ugarte, Laboratório Nacional de Luz Síncrotron (CNPq/MCT), Caixa Postal 6192, 13083-970 Campinas SP, Brazil.
A. Châtelain, Institut de Physique Expérimentale, Département Physique, Ecole Polytechnique Fédérale de Lausanne, 1015 Lausanne, Switzerland.
W. A. de Heer, School of Physics, Georgia Institute of Technology, Atlanta, GA 30332, USA.

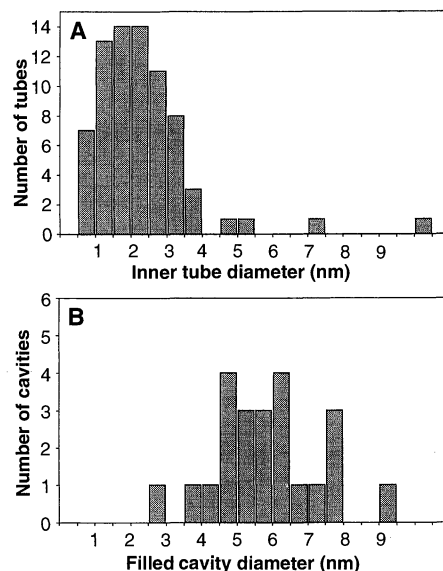*To whom correspondence should be addressed. E-mail: ugarte@LNLS.BR

Fig. 1. (A) Histogram of the diameter distribution of the inner cavity of arc-generated multilayered carbon nanotubes (74 tubes); (B) Inner diameter distribution of filled nanotubes (26 tubes).